CHAPTER – 4

LOCAL COMPOSITION MODULATION AND ORIENTED INTER-GROWTH INDUCED STRAIN MINIMIZATION IN ENTROPY STABILIZED (CoCuMgNiZn) OXIDE

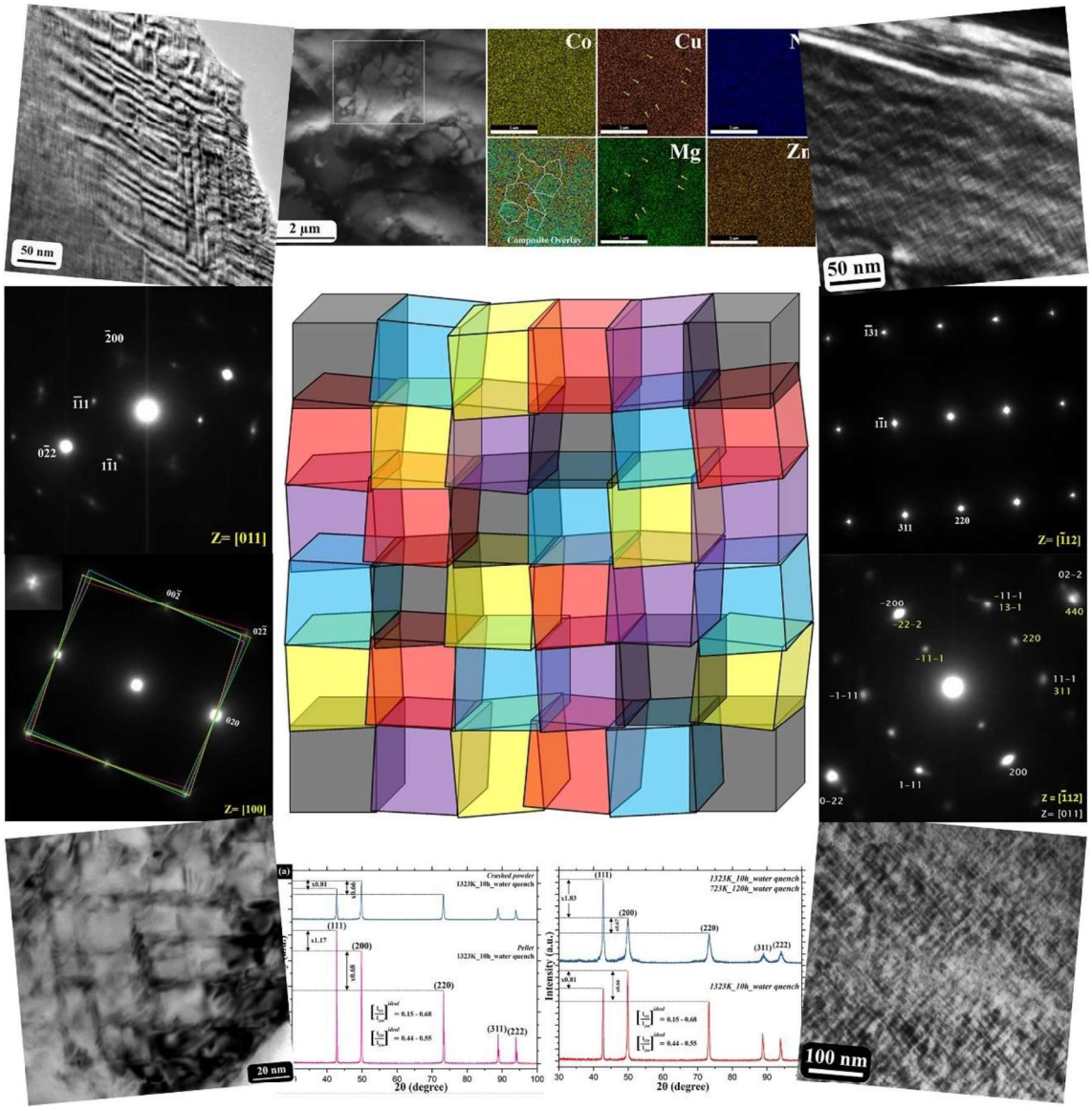

4.1. Introduction

High entropy materials/ceramics (HEMs/HECs) [1-2] have emerged over the last decade as a potential candidate for catalysis, electrochemical energy conversion and storage [3-7]. High entropy oxides (HEOs) [8-9] are one of the important members in the family of HEMs/HECs. They differ from high entropy alloys (HEAs) [10-11], as in case of HECs/HEOs, there are distinct sublattices for cations and anions [12-14]. The entropy of the materials may be made high either by the substitution of cations or anions or both in their respective sublattices in equimolar or near equimolar proportions [15]. As a result, the calculation of total entropy is also done separately for cation and anion sublattice for HEOs/HECs. It is also believed that little difference in the ionic sizes coupled with negative enthalpy of mixing and isostructuralism of most of the precursors are promoting factors for synthesis of stable, single-phase HEOs/HECs [16]. Presence of multiple ions in the cation or anion sublattice makes the configurational entropy so high that this class of materials are always stabilized by entropy, which has led to the derivation of their new name as entropy stabilized materials (ESMs) [12].

(CoCuMgNiZn) high entropy oxide is the first known ESO in this class, which is stabilized in a cubic rocksalt structure [12, 17]. A good volume of data has been reported on the synthesis and functional properties of this ESO [18-20]. However, its mechanism of entropic stabilization, distribution of cations, stability in the time-temperature space and tailoring of novel properties upon further substitution has received relatively less attention [13, 15, 21-22]. An atomistic picture that combines its structure, stability and properties is still missing.

The present work has been taken up to synthesize single-phase ESO in equimolar (CoCuMgNiZn) system and study its local structure, chemistry and stability in the time-temperature space so that the atomic scale mechanisms behind the evolution of novel

properties may be deciphered and tailored further. It is observed that the ESO forms a cubic rocksalt structure globally. However, there are modulated domains within the structure and there is a definite tendency of the ESO to minimize its volumetric, lattice and interfacial strain through the formation of tweeds, domains and inter-growth of structurally correlated phases, which is presented in the subsequent sections of the communication.

4.2. Materials & methods

Multicomponent, equimolar (CoCuMgNiZn) entropy stabilized oxide has been prepared through solid state synthesis route pertaining to the ease of materials handling and probability of success. High purity metal oxide; Co(II, III)O (>99.8 at%), CuO (>99.9 at%), MgO (>99.95 at%), NiO (>99.9 at%) and ZnO (>99.95 at%) were procured from either Sigma Aldrich or Alfa Aesar. Metal oxides in stoichiometric proportions were mixed thoroughly in a mortar and pestle. The mixed powder was compacted in a uniaxial hydraulic press with 4T load to form the green compacted pellets of ~12 mm diameter and ~4-5 mm thickness. The green compacted pellets were sintered in a high temperature tube furnace in air to obtain the entropy stabilized (CoCuMgNiZn) oxide. In order to maintain perfect stoichiometry and avoid contamination, a number of green compacted pellets were vertically stacked in a platinum crucible with the lid on. The sintered pellet from the center of the stack, in all the heat treatments, was taken for further studies. Four different heat treatment schedules for sintering the green compacted pellets to form the entropy stabilized (CoCuMgNiZn) oxide was followed. Those are; sintering at 1323 K for 10 h followed water quenching, sintering at 1323 K for 100 h followed by water quenching, sintering at 1323 K for 10 h followed by furnace cooling to room temperature at ~3 ^{o}C/min and sintering at 1323 K for 10 h followed by ageing at 723 K for 120 h and subsequent water quenching.

Phase evolution in the sintered samples in pellet and powder form were studied by x-ray diffraction (XRD) in a Malvern Panalytical Empyrean high-resolution x-ray diffractometer

with Cu-K_α (λ= 1.54 Å) and Co-K_α (λ= 1.79 Å) radiation. The diffractometer was operated at 40 kV operating voltage with 40 mA tube current. Prior to the x-ray diffraction experiments of the pellets, both sides of the pellet were polished in a conventional way. Microstructure and chemistry of the sintered pellets were studied in a FEI Quanta 200F scanning electron microscope (SEM) operated with an accelerating voltage of 30 kV. For SEM studies the sintered, aged and quenched pellets were metallographically polished and ultrasonicated in ethanol. X-ray energy dispersive spectroscopy (XEDS) mapping of the samples was done at the regions of interest in order to understand the distribution of the ions. The sintered, aged and quenched samples of the entropy stabilized (CoCuMgNiZn) oxide were studied in a FEI Tecnai G2 T20 transmission electron microscope (TEM) under 200 kV accelerating voltage. For TEM observation, the sintered, aged and quenched samples were cut into thin slices by using a low-speed diamond saw, then they were polished to a minimal thickness of ~100 μm, dimple ground to ~30 μm and then they were thinned to electron transparency by PIPS II Gatan ion mill.

The simulation of x-ray diffraction patterns was done by indigenously developed code and JEMS software was used for simulation of electron diffraction patterns. VESTA software was used for development of crystal structure models.

4.3. Results

X-ray diffraction (XRD) patterns with Co-K_α (λ= 1.79 Å) radiation from the (CoCuMgNiZn) entropy stabilized oxide (ESO) after sintering at 1323 K for 10 h followed by water quenching are given in Figure 4.1a. The XRD pattern (in pink) from the sintered quenched pellet shows sharp 111, 200, 220, 311 and 222 peaks corresponding to a rocksalt structure with *a~4.24 Å* lattice parameter. The sharp diffraction peaks are indicative of strain free grains with large grain size. In this diffraction pattern shouldering of the 220, 311 and 222 peaks can be observed. Shouldering of the peaks in an ESO with exactly similar composition has been observed before, which has been attributed to the diffraction by $K_{\alpha II}$ radiation of the target material [17]. However, it could be due to the introduction of tetragonality in the otherwise (CoCuMgNiZn) ESO with cubic rocksalt structure or local modulation in the d-spacings in the crystal. It has also been investigated with electron diffraction and will be discussed later in this communication. The XRD pattern (in blue) from the sintered, quenched (1323 K for 10 h) and powdered sample shows similar diffraction peaks with minor right shift, which can be indexed to a rocksalt phase with *a~4.23 Å* lattice parameter. In this sample, the diffraction peaks are quite sharp indicative of large strain free crystals in the microstructure. In this diffraction pattern also shouldering of the peaks at higher angle could be observed. In comparison to the diffraction pattern from the pellet (in pink), the diffraction peaks from the powder sample are relatively broad. Additionally, a reversal in the total integrated intensity of 111 and 200 peaks in the pellet and the powder sample is easily discerned. In the pellet (in pink), the total integrated intensity of the 111 peak is ~1.17 times of that of the 200 peak. However, the total integrated intensity of the 111 peak in the powder sample (in blue) is ~0.81 times of the 200 peak.

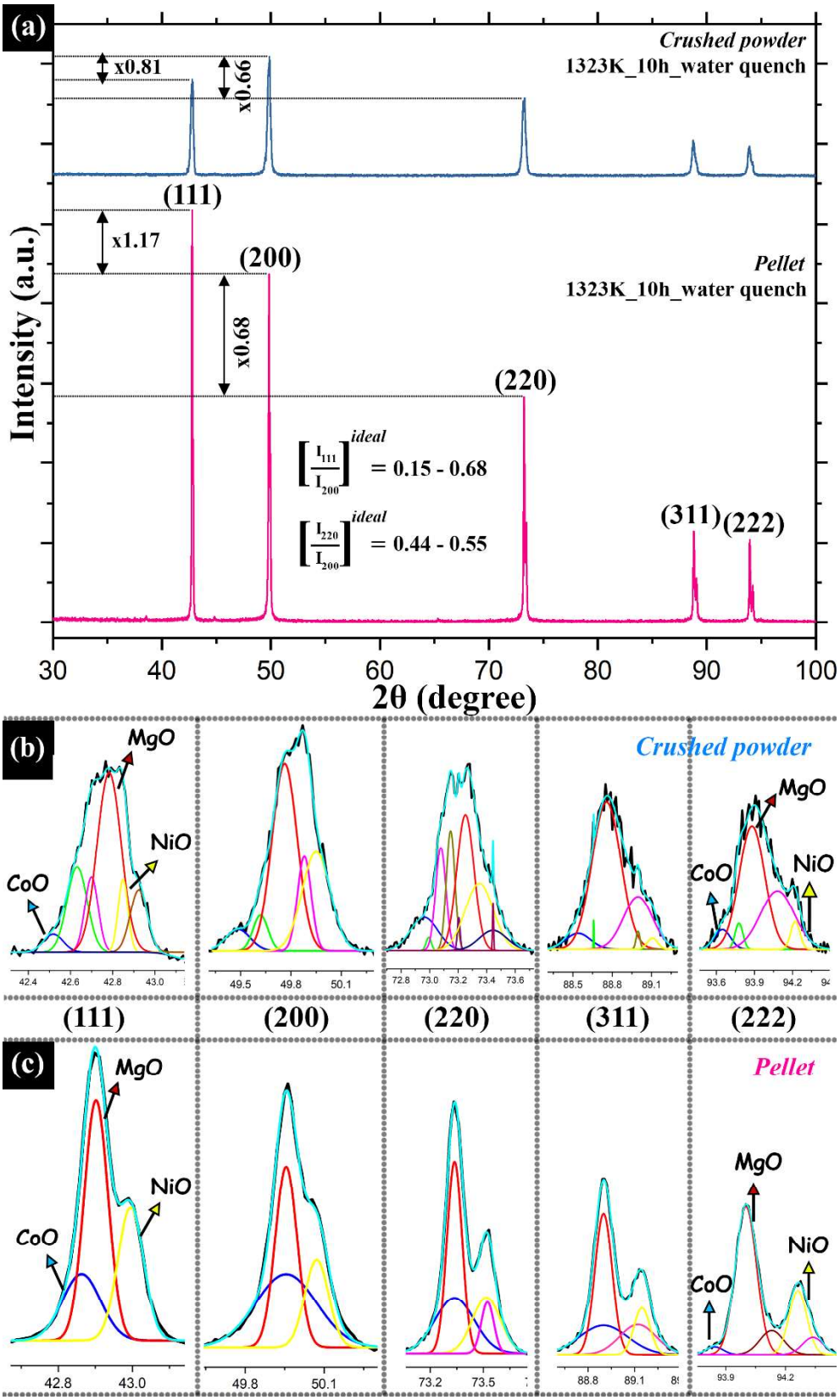

Figure 4.1: (a) X-ray diffraction (XRD) patterns of (CoCuMgNiZn) ESO after sintering at 1323 K for 10 h followed by water quenching. The diffraction pattern in pink is from the sintered and quenched pellet and the pattern in blue is from its crushed powder. (b) Deconvolution of the XRD peaks from the crushed powder and (c) deconvolution of the XRD peaks from the pellet. Deconvoluted peaks can be matched with CoO, MgO and NiO.

The ideal intensity ratio of 111 and 200 diffraction peak from a typical rocksalt structure should be ~0.15-0.68 (as obtained from simulation and reported JCPDS data cards), which is closely observed in the powder. In fact, it is worth mentioning that none of the intensity ratios in the diffraction pattern from the pellet and the powder match with the ideal intensity ratios for a cubic rocksalt structure. The reversal in intensity in case of the pellet may be attributed to the development of a weak surface texture. It is also reported that in this ESO, reversal of intensity may appear due to the distortion in the structure induced by Jahn-Teller distortion and processing history [23, 24]. The departure of the diffraction patterns from the ideal diffraction pattern of a cubic rocksalt structure is indicative of the presence finer structural modulations, which is worth probing further.

In order to probe the presence of finer structural details in the sintered and quenched (1323 K for 10 h) (CoCuMgNiZn) ESO, all the XRD peaks from the powder and the pellet have been deconvoluted (Figure 4.1(b-c)) and each of the deconvoluted peaks has been matched against individual oxide precursors used for the synthesis of the ESO. The XRD peaks from the powder sample (Figure 4.1b) are relatively broad with several discontinuities. All the diffraction peaks may be deconvoluted to several major and minor peaks with the left most one (blue), middle one (red) and right most one (yellow) matching with CoO, MgO and NiO respectively. Similar trend is observed in the XRD peaks from the pellet sample. The XRD peaks from the pellet may be deconvoluted (Figure 4.1c) to three major peaks; the left most (blue), middle (red) and right most (yellow) may be indexed with the corresponding d-spacings of CoO, MgO and NiO respectively. Deconvolution of the XRD peaks and its similarity with the corresponding d-spacings of the pure precursor oxides hints at local composition variation that may exist in this otherwise cubic rocksalt based ESO. It may further be inferred that local modulation of the structure, caused by local composition variation, is very much akin to the rocksalt structures of CoO, MgO and NiO.

Copper and zinc ions are incorporated into the local structure. Introduction of copper and zinc may further introduce distortion and Jahn-Teller effect, which is manifested by the presence of shouldering and non-ideal intensity distribution in the XRD pattern.

XRD patterns of the (CoCuMgNiZn) ESO pellet after sintering at 1323 K for 10 h followed by water quench, sintering at 1323 K for 100 h followed by water quench and

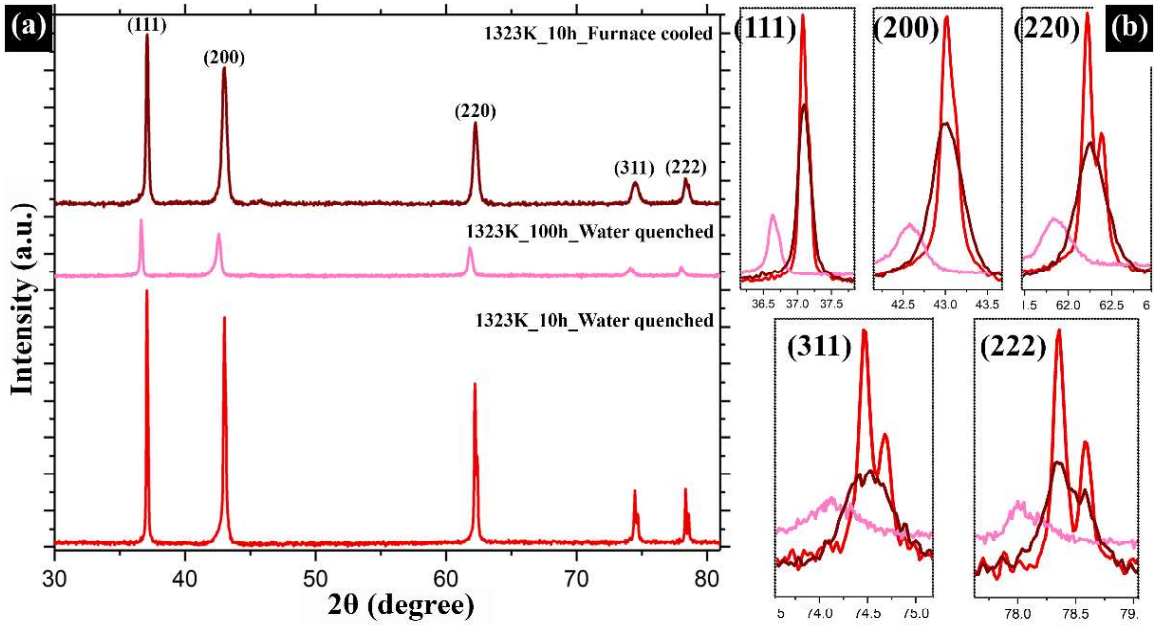

Figure 4.2: (a) X-ray diffraction patterns (XRD) of (CoCuMgNiZn) ESO pellet after sintering at 1323 K for 10 h followed by water quenching (red), after sintering at 1323 K for 100 h followed by water quenching (pink) and after sintering at 1323 K for 10 h followed by furnace cooling (brown). (b) Superimposition of XRD peaks after three different thermal treatments. Long h of exposure at high temperature leads to a systematic left shift coupled with broadening and reduction in total integrated intensity.

sintering at 1323 K for 10 h followed by furnace cooling at ~3°C/min are given in Figure 4.2a. The x-ray diffraction experiments were conducted by Cu-K_α radiation ($\lambda_{Cu\ K\alpha}$ = 1.54 Å). All the diffraction patterns may be indexed with cubic rocksalt structure with subtle differences. In the diffraction pattern from the pellet after sintering at 1323 K for 10 h sharp peaks with clear shouldering in the higher angle peaks could be observed. However, in the diffraction patterns, after sintering for 100 h followed by water quenching and sintering for 10 h followed by furnace cooling, shouldering is not clearly visible and the diffraction

peaks have broadened instead. Broadening of the diffraction peaks after longer h of sintering and after furnace cooling is counter-intuitive as longer h of exposure at high temperature should release the strain in the sample and corresponding grain growth should result in sharpening of the peaks. In order to rationalize this observation, the diffraction peaks after three heat treatment cycles are superimposed (Figure 4.2b). It is observed that for samples after sintering at 1323 K for 10 h the diffraction peaks (in red) are the most intense ones. After sintering at 1323 K for 10 h followed by furnace cooling there is no shift in peak position (in brown), however there is a broadening induced reduction in the peak intensity. This observation indicates that longer h of exposure at high temperature results in more variation in the d-spacings of the same crystal structure, which is intuitively indicative of a local fine scale composition modulation that is likely to induce a change in the structure parameters of the crystal. It will be probed further in the later sections of the communication. A clear left shift in the peak positions along with broadening induced reduction in total intensity of the peaks (in pink) is observed after sintering the ESO at 1323 K for 100 h. Broadening of the peaks with associated reduction in the total intensity may be explained by the local fine scale composition modulation induced structural changes leading to a wider variation in the d-spacings. However, the left shift of the peaks indicates an additional increase in the average cell parameter and the cell volume. Increase in average cell parameter and its volume may be directly correlated with reduction in the volumetric strain in the crystal as the increase in the crystal volume necessarily means increase in size of the octahedral voids and easier accommodation of the cations in there in an ideal rocksalt structure. It will be discussed further and will be associated with the stabilization of the ESO in later part of the communication.

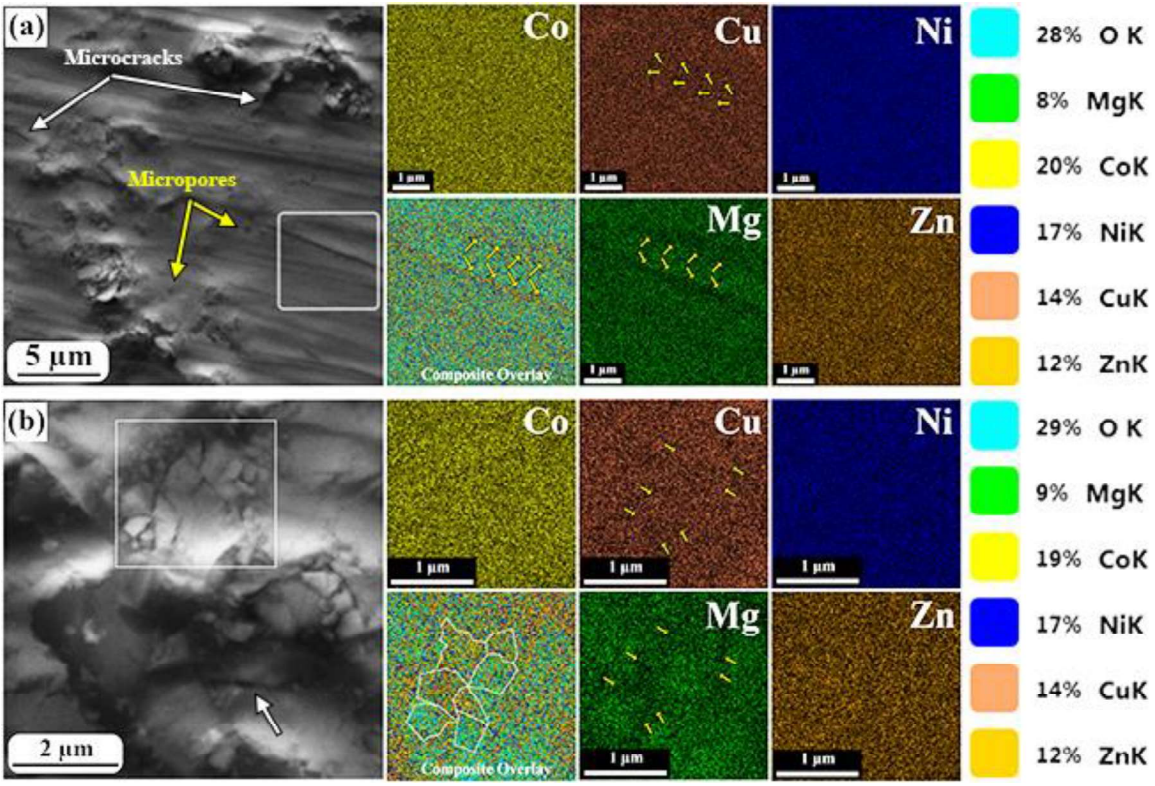

Figure 4.3: Scanning electron microscope (SEM) image and XEDS chemical maps of Co, Cu, Mg, Ni, Zn and the composite map of (CoCuMgNiZn) ESO pellet after (a) sintering at 1323 K for 10 h and (b) 1323 K for 100 h followed by water quenching. Fine scale segregation of Cu and Mg ions is evident in the maps. It is marked with arrows and delineated with dotted boundaries.

Secondary electron image and X-ray energy dispersive spectroscopy (XEDS) maps of all the ions in the (CoCuMgNiZn) ESO after sintering at 1323 K for 10 h and 100 h are given in Figure 4.3(a-b) respectively. In the secondary electron image of the ESO after sintering at 1323 K for 10 h (Figure 4.3a), uniformly sintered grains with varying grain sizes is observed. In the image, a few scattered pores and microcracks (marked with arrows) are also observed. In the XEDS maps, Co, Ni and Zn ions are uniformly distributed. However, local segregation of Cu and Mg is easily discerned (marked with arrows). The Cu ion enriched regions are depleted in Mg ions and vice versa. In the composite map of all the ions, clearly delineated colour distribution indicates that microscale chemical segregation of Cu and Mg takes place after 10 h of sintering at 1323 K in this ESO. (CoCuMgNiZn) ESO has been reported to form chemically homogeneous single phase [12, 17]. However,

microscale chemical segregation is clearly evident in this system. The same ESO after sintering at 1323 K for 100 h (Figure 4.3b) continues to maintain the grainy morphology with a wide variation in grain size. In the XEDS maps, a fairly uniform distribution of Co, Ni and Zn ions can be readily discerned over a large scale. However, there are isolated regions (marked with arrows) where Cu and Mg ions are preferentially segregated at sub-micron length scales. In the composite map, sub-grain boundaries have been delineated, where sub-grains preferentially enriched in Cu or Mg ions are observed. This observation, contrary to published literature reports [12, 17], proves that chemical segregation takes place in this ESO and the segregated regions grow in size with the time of sintering. However, the kinetics of chemical segregation and grain growth appears to be quite sluggish.

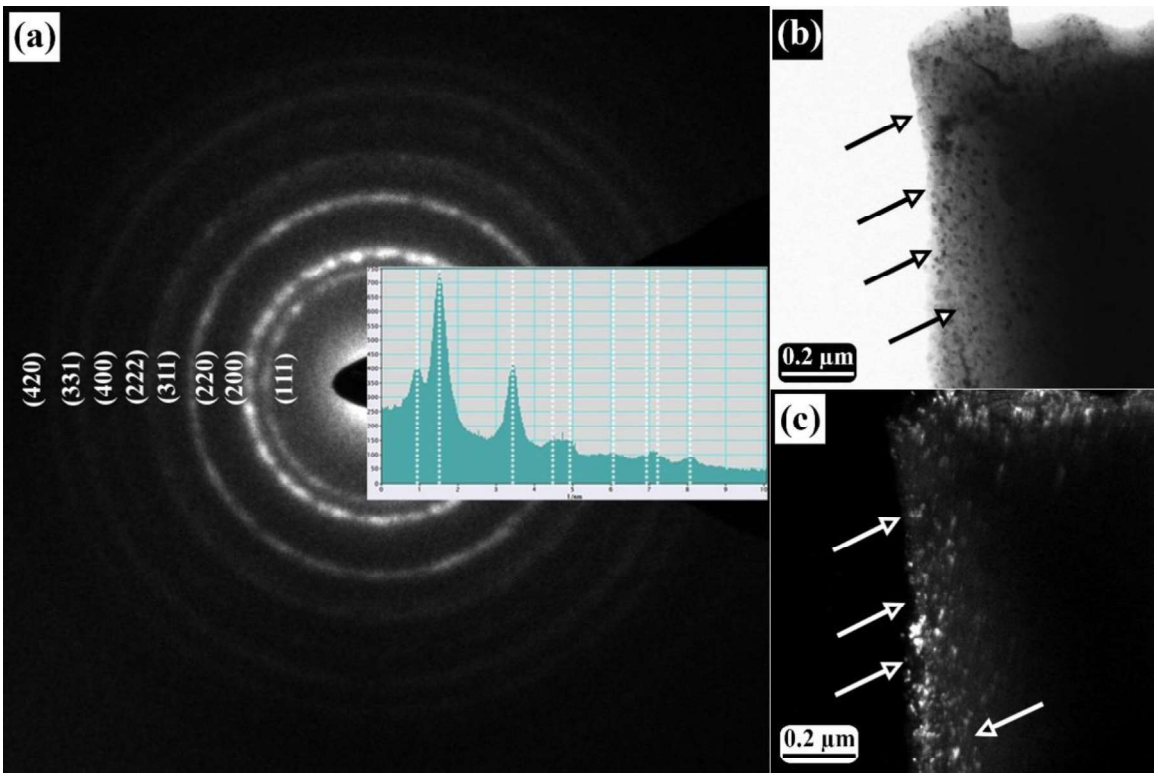

Figure 4.4: Sintered and quenched equimolar quinary (CoCuMgNiZn)ESO exhibiting (a) Polycrystalline electron diffraction pattern with spotty rings which can be indexed to a FCC phase with a~4.23 Å lattice parameter whereas (b) and (c) are the corresponding BF-DF pair showing nano-crystallites of the rocksalt phase. It was recorded from the periphery of the sample after ion-milling, making it necessary to revisit and optimize the electron thinning parameters to avoid such process-induced particle size refinement.

Selected area electron diffraction pattern with its corresponding bright field and complimentary dark field images of the sintered and quenched (CoCuMgniZn) ESO is shown in Figure 4.4(a-c). The diffraction pattern brings out the polycrystalline nature of the ESO, which shows concentric spotty rings that may be indexed to a FCC structure with $a \sim 4.2$ Å (marked in Figure 4.4a). The intensity line profile when plotted along the radius of the circles, gives rise to all the allowed reflections of the cubic rocksalt phase. Corresponding BF/DF pair shows the presence of nano-crystallites of the rocksalt phase, which undergoes reversal of contrast from dark spots in BF to illuminated bright spots in the complimentary DF image (marked with arrows in Figure 4.4b-c). However, in order to probe single-crystal diffraction patterns for further insights, the ion-milling parameters were optimized to reduce such process-induced particle size refinement.

Bright field TEM images and selected area electron diffraction patterns from different zone axes of the (CoCuMgNiZn) ESO after sintering at 1323 K for 10 h followed by water quenching are given in Figure 4.5(a-f). The electron diffraction patterns (Figure 4.5(a-d)) may be indexed to a cubic rocksalt structure with $a \sim 4.22$ Å, which is in agreement with the lattice parameter value as obtained from the XRD patterns. Some of the diffraction spots are diffused, streaked and occasionally a shape is observed (marked by dotted circles in Figure 4.5(a-d)). In the bright field image (Figure 4.5e) large faceted grains with fringe contrast at the grain boundaries is observed. However, within the grain a tweed like contrast is observed, which is not expected in single-phase materials with uniform chemistry. Higher magnification image (Figure 4.5f) of the grain body shows an inter-weaved pattern. The size of the inter-weaved regions is ~5-15 nm. However, there are regions in the grain body, which are free from such tweed-like structures. It is marked with a faceted boundary structure. The tweeds are wavy and the tweed boundaries are not perpendicular to one another (Figure 4.5f).

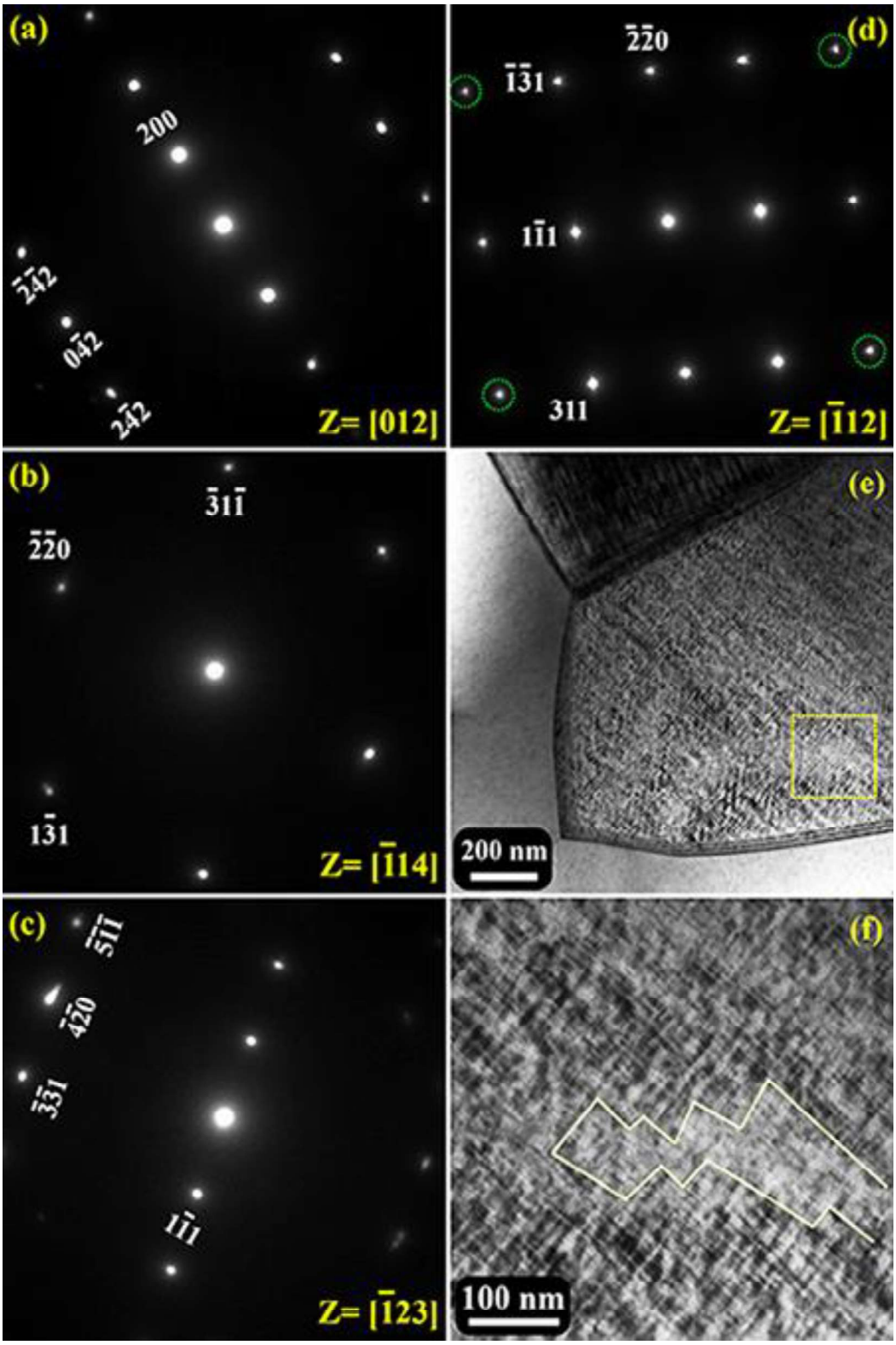

Figure 4.5: (a-d) Electron diffraction patterns of (CoCuMgNiZn) ESO after sintering at 1323 K for 10 h followed by water quenching. The electron diffraction patterns are from (a) z=[012], (b) z=[$\bar{1}$14], (c) z=[$\bar{1}$23], (d) z=[$\bar{1}$12]. In the bright field image in (e) tweed contrast within the grain body and fringe contrast at the grain boundaries is observed. (f) Magnified image of the region marked with dotted square in (e). Tweed free region is marked with yellow lines.

The origin of this inter-woven tweed morphology could be due to the oriented growth of polymorphically related structures within the same grain with or without any modulation in chemistry. However, in the secondary electron images and in the XEDS chemical maps, fine scale chemical segregation has been observed (Figure 4.3). It is expected that the tweed morphology evolves out of a fine scale chemical modulation induced polymorphic transformations within the grain body. It requires further investigation and it will be reported in subsequent sections of the communication.

Selected area electron diffraction pattern from one large and faceted grain of (CoCuMgNiZn) ESO after sintering at 1323 K for 10 h followed by water quenching may be indexed to a [100] zone axis pattern of a cubic rock salt structure with $a \sim 4.22$ Å lattice parameter (Figure 4.6a). However, there are finer details in the pattern, e. g. 020 type spots are streaked along two almost perpendicular directions and there is diffuseness around the spots. The 022 type of spots show intensity modulation along two almost perpendicular directions and there is diffused streaking around it (Figure 4.6a inset). Intensity modulation leading to a particular shape of the diffraction spots and diffused streaking clearly indicates local modulation in d-spacings in the crystal. In order to rationalize the observation, extreme ends of the intensity modulations are joined together with dotted coloured lines (Figure 4.6a), which bring out the [100] zone axis symmetry shapes of a cubic rocksalt structure, however mutually rotated with respect to one another. Individual differently coloured [100] zone axis symmetry shapes are given in Figure 4.7a. The symmetry shapes may be divided into two sets (blue, pink form one set and green, yellow form another set), in each set the symmetry shapes are rotated in opposite sense, however by varying degrees. From each of these symmetry shapes, when 002 and 020 type vectors are plotted (Figure 4.7b), it appears that the magnitude of ratio of 002 and 020 vectors for the blue and pink pair is ~1, however the same ratio is ~1.02 for the green and

yellow pair. This definitely indicates that there could be local composition modulation induced distortions in the crystal. To support this point further the angular relationships between the 002 and 020 type vectors have been looked at and it has been found to be not exactly 90°.

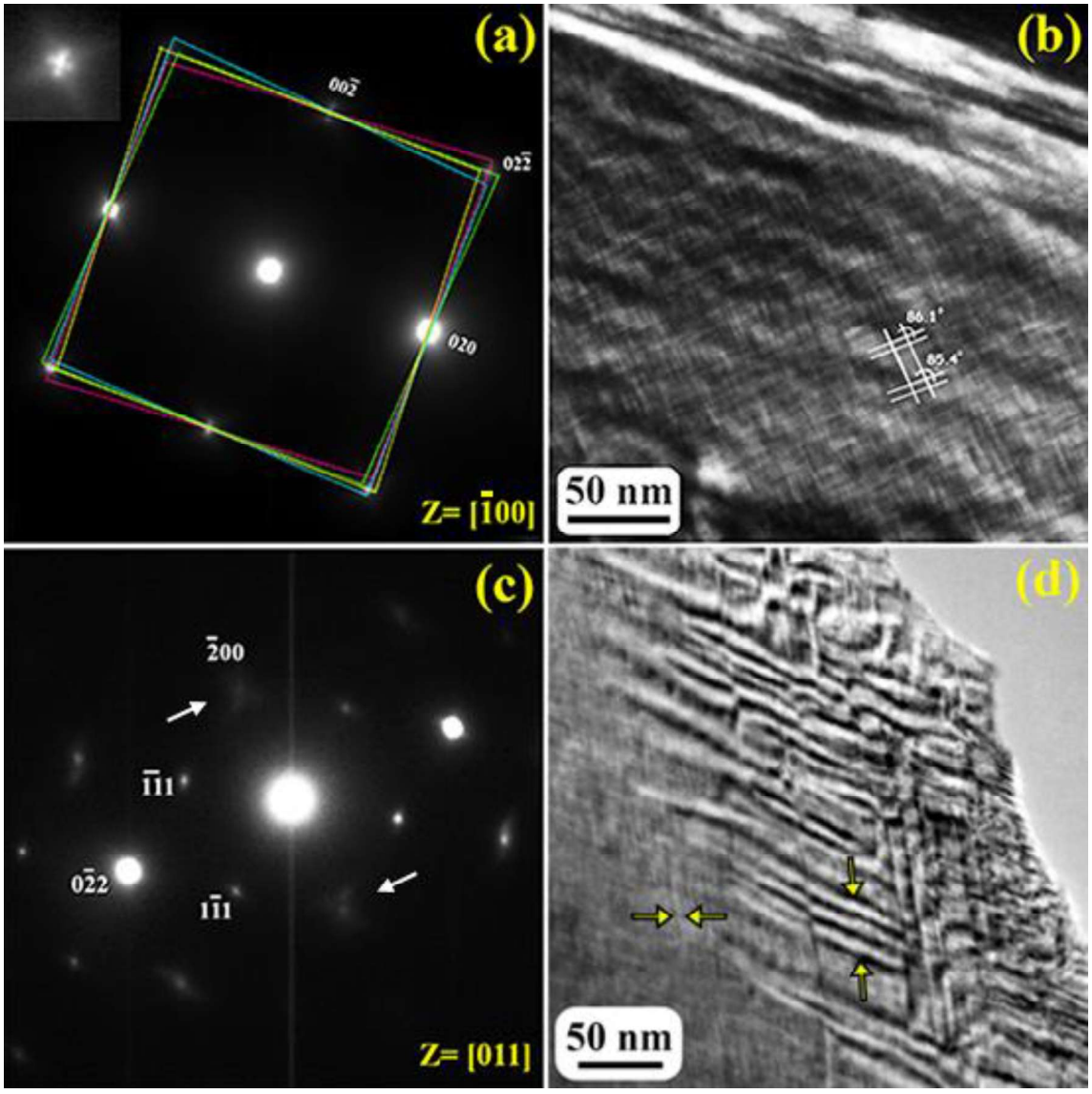

Figure 4.6: (a-d): Electron diffraction patterns, bright and dark field images of (CoCuMgNiZn) ESO after sintering at 1323 K for 10 h followed by water quenching. The diffraction pattern in (a) corresponds to z=[1̄00] zone axis pattern of a cubic rocksalt structure. Diffused scattering, streaking and shape evolution (inset) of 022̄ type spot is observed. Extreme ends of the modulated spots are joined together to reveal the mutually rotated symmetry shapes. In the dark field image in (b) mutually intersecting non-orthogonal tweeds are observed. The electron diffraction pattern in (c) is from z=[011] zone axis of the same grain, where streaking and diffused intensity of the spots is observed. The bright field image in (d) shows the inter-penetrating tweeds.

This further indicates that local composition fluctuation induced non-cubic distortions take place in the crystal, and that in turn leads to shape evolution in the diffracted spots. The size of the modulated domains is so small that it gives birth to streaking in perpendicular directions. The structure of this phase largely remains to be cubic rocksalt globally, when such fine details in the diffraction pattern are ignored. However, such fine scale modulations are definitely present in the crystal and they manifest themselves in terms of shape evolution of the diffracted spots. When individual and differently coloured [100] symmetry shapes with their relative rotation and distortion are superimposed (Figure 4.7c), it gives rise to the experimentally observed diffraction pattern in Figure 4.6a. It is worth noting at this point that, such kind of composition modulation may not be detected by high resolution chemical mapping as chemically modulated domains are randomly distributed in the crystal and even fine probe techniques will not be able to detect the small variations in local chemistry within the individual domains due to the finite thickness of the crystal.

Dark field TEM image from the grain body (Figure 4.6b) with the 020 spot in the diffraction pattern in Figure 4.6a clearly brings out the tweed contrast in the grain interior. The individual tweeds are wavy but continuous and they do not intersect each other in exactly perpendicular orientation (marked by the traces in Figure 4.6b). This perfectly corroborates the experimentally observed diffraction pattern (Figure 4.6a) and its theoretical interpretation (Figure 4.7). Selected area electron diffraction pattern from the same grain along [011] zone axis (Figure 4.6c) exhibits similar shape evolution and streaking of 200, 022 and 222 type of spots. Similar wavy and mutually intersecting tweeds are observed in the bright field image (Figure 4.6d). Similar and mutually corroborating evidence in real and reciprocal space from two different major zone axis directions of the same grain definitely proves local composition modulation and distortion in the crystal after sintering and quenching.

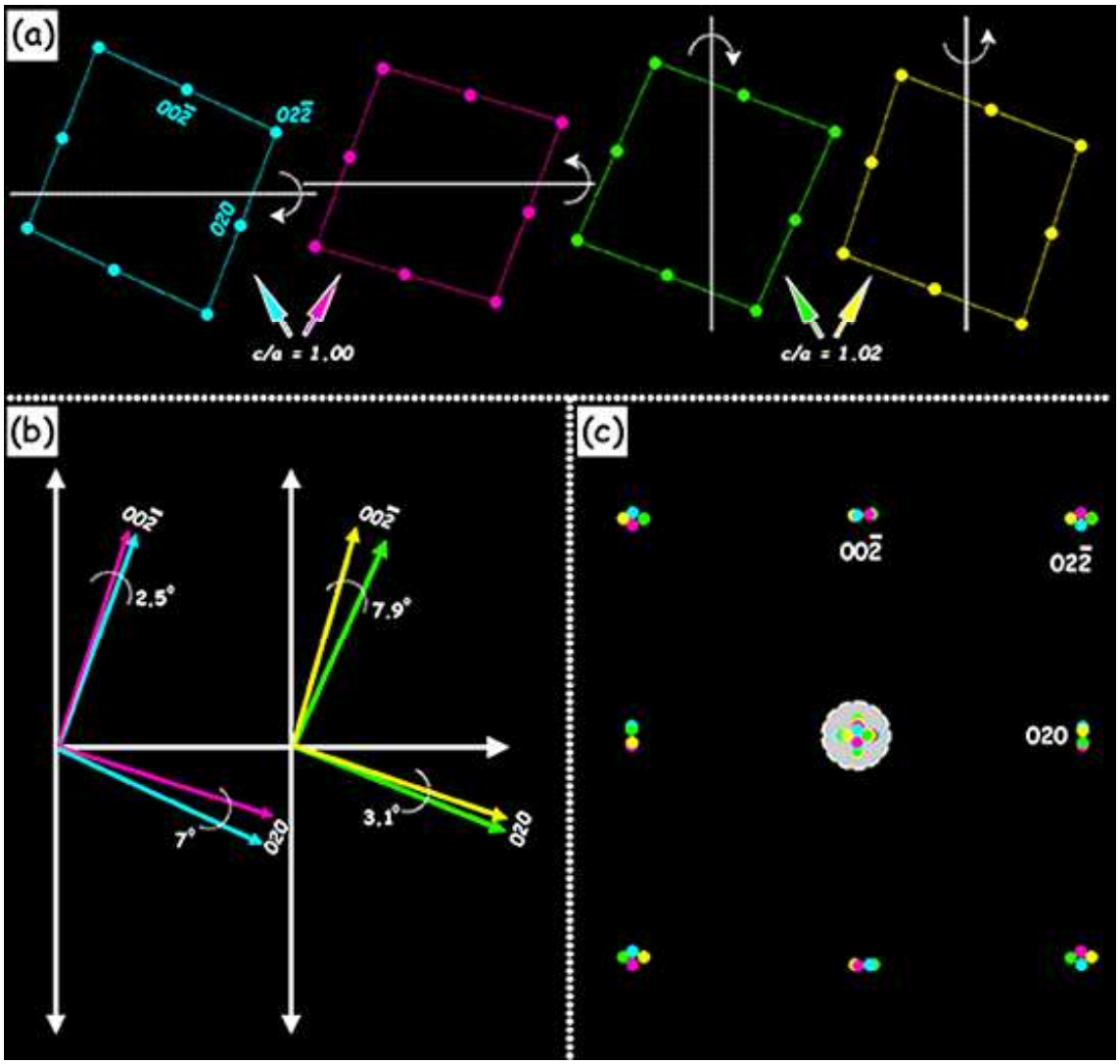

Figure 4.7: (a) Mutually rotated symmetry shapes as obtained from the electron diffraction pattern in Figure 5(a). The symmetry shapes may be separated into two groups with mutual relative rotation and with different c/a ratios. (b) Principal vectors from the symmetry shapes in (a) are plotted to reveal their relative rotation. (c) Mutually rotated symmetry shapes in (a) are superimposed to schematically generate the electron diffraction pattern in Figure 5(a).

Selected area electron diffraction patterns and corresponding bright field images from a different region of the (CoCuMgNiZn) ESO after sintering at 1323 K for 10 h followed by water quenching are given in Figure 4.8(a-d). The diffraction pattern in Figure 4.8a, may be indexed to a [100] zone axis pattern of a cubic rocksalt structure with *a~4.23 Å* lattice parameter, which is exactly similar to the lattice parameter as obtained from the XRD studies. However, in the diffraction pattern, the 002 type of spots are elongated and the 220

type of spots are arced with a definite intensity modulation. The two extreme ends of the arced reflections are connected by dotted cyan and yellow lines, which bring out two mutually rotated symmetry shapes of [100] zone axis of a cubic rocksalt structure. Similar such symmetry shapes may be generated by connecting all the in between spots of the arced 220 type of reflections. It may be inferred from this observation that several cubic domains with mutual in-plane rotation gives birth to such arced reflection in the diffraction pattern. In the corresponding bright field image (Figure 4.8b) mottled contrast with parallel linear fringes (marked with arrows) may be observed. Combined observation of arcing in the diffraction pattern (Figure 4.8a) and mottled contrast with linear fringes in the bright field image (Figure 4.8b) corroborates to the fact that several mutually rotated domains exist in the grain. In order to reduce the interfacial strain, the domains rotate with respect to one another. Selected area diffraction pattern from the same grain but along [$\bar{1}$12] zone axis (Figure 4.8c) exhibits similar elongation and arcing of the diffraction spots with definite intensity modulation. When the extreme ends of the arced spots are connected together by dotted cyan and yellow lines, mutually rotated symmetry shapes of [$\bar{1}$12] axis are observed. In the corresponding bright field image (Figure 4.8d) mottled contrast with linear fringes is observed. It further reinforces the fact that mutually rotated cubic domains do exist in the ESO. As arcing is observed from two not mutually perpendicular zone axes, it is confirmed that the domains are having both in-plane and out-of-plane rotation. It arises out of the tendency of the material to reduce strain, which will be elucidated further in the discussion section.

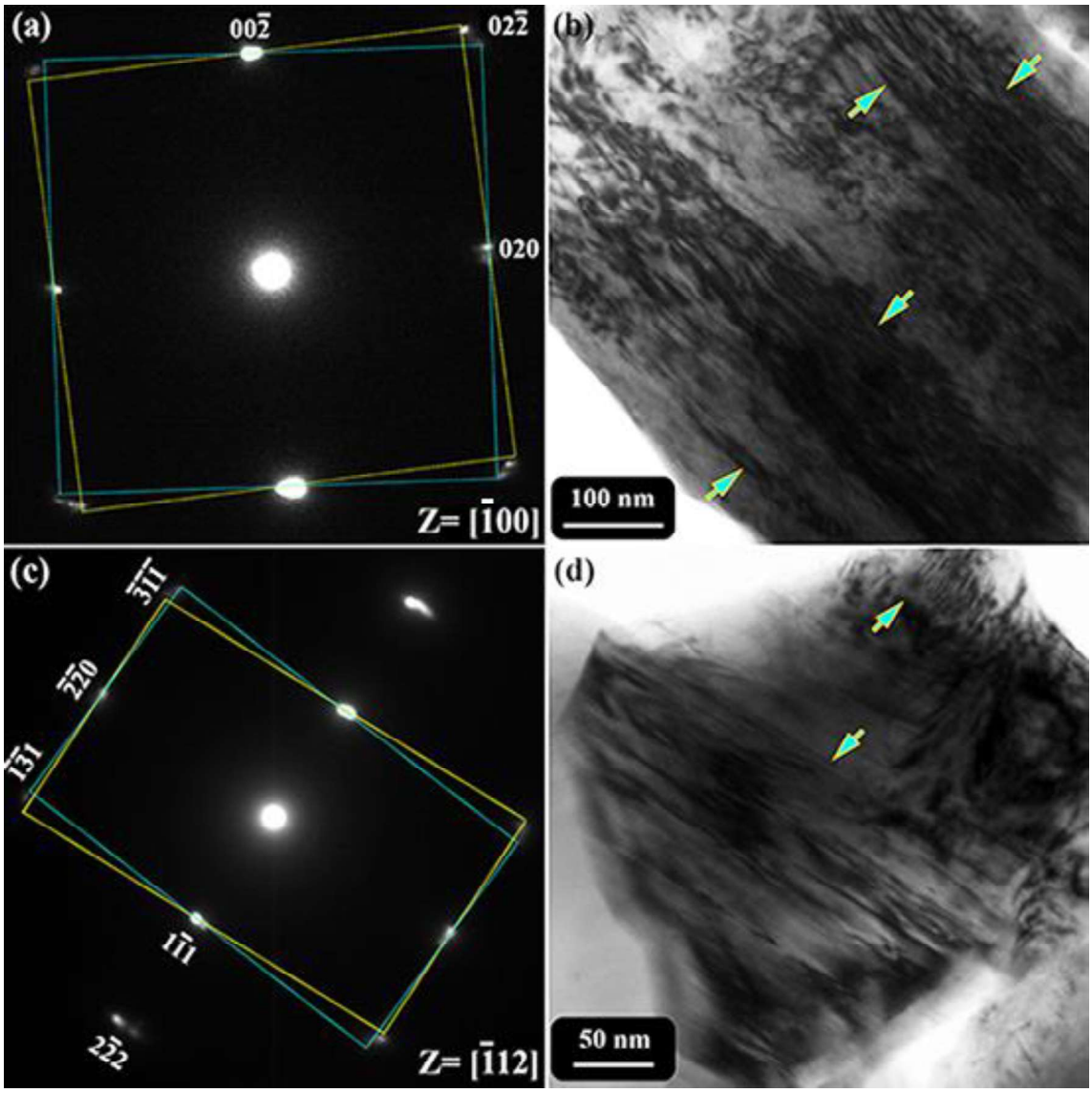

Figure 4.8: (a-d): Electron diffraction patterns and TEM bright field images of (CoCuMgNiZn) ESO after sintering at 1323 K for 10 h followed by water quenching. Arcing in (a) z=[$\bar{1}$00] and (c) z=[$\bar{1}$12] electron diffraction patterns is associated with the mutual in-plane and out-of-plane rotation of domains. Intensity modulated arcs in each of the diffraction patterns are connected with dotted lines to reveal the symmetry shapes of the corresponding zone axes. Fringe contrast is observed in corresponding bright field images in (b) and (d). The fringes are marked with arrows.

XRD pattern of the (CoCuMgNiZn) ESO powder after sintering at 1323 K for 10 h followed by water quenching (in red) and the same powder after sintering at 1323 K for 10 h followed by ageing at 723 K for 120 h followed by water quenching (in blue) are given in Figure 4.9. The x-ray diffraction experiments were conducted by Co-K_α radiation ($\lambda_{Co\ K\alpha}$ = 1.79 Å). As observed previously, in the XRD pattern of the sintered and quenched ESO

powder the diffraction peaks are sharp and they may be indexed to a cubic rocksalt structure with *a~4.23 Å* lattice parameter. Minor shouldering is observed in the diffraction peaks, which may be attributed to local composition modulation induced variation of d-spacings or introduction of tetragonality in the crystal. The ratio of the integrated intensity of 111 and 200 peaks is ~0.81, which is close to the ideal value. In the XRD pattern of the same ESO powder after ageing at 723 K for 120 h, similar peaks corresponding to a cubic rocksalt structure are observed. However, the peaks are broad, which is counter intuitive. The broadening of the peaks may be attributed to the development of a wider variation in d-spacings in the crystal upon ageing. It has been investigated further by electron diffraction and diffraction contrast imaging. After ageing the sample, reversal of 111 and 200 peak intensities is observed. The integrated intensity ratio of 111 and 200 peak after ageing the ESO turns out to be ~1.83. Reversal in intensity ratio in ESOs has been attributed to the processing history and active interplay of Jahn-Teller distortion [23]. The microstructural effect of this has been investigated by diffraction contrast imaging.

Selected area electron diffraction pattern from [100] zone axis of the (CoCuMgNiZn) ESO after sintering at 1323 K for 10 h followed by ageing at 723 K for 120 h and water quenching (Figure 4.10a) shows spot splitting and asymmetric diffused scattering. Spot splitting and diffused scattering clearly indicates the formation of structurally related domains with possible minor rotation among them. The diffraction pattern may be indexed as a whole to a cubic rocksalt structure with *a~4.23 Å* lattice parameter. However, it is not possible to determine the variation in crystal structure and lattice parameter of individual domains with accuracy. In the corresponding bright field image (Figure 4.10b) interpenetrating boundaries leading to a domain-like structure are observed. In the higher magnification image of the same area (Figure 4.10c) almost square domains of ~15-25 nm size are observed.

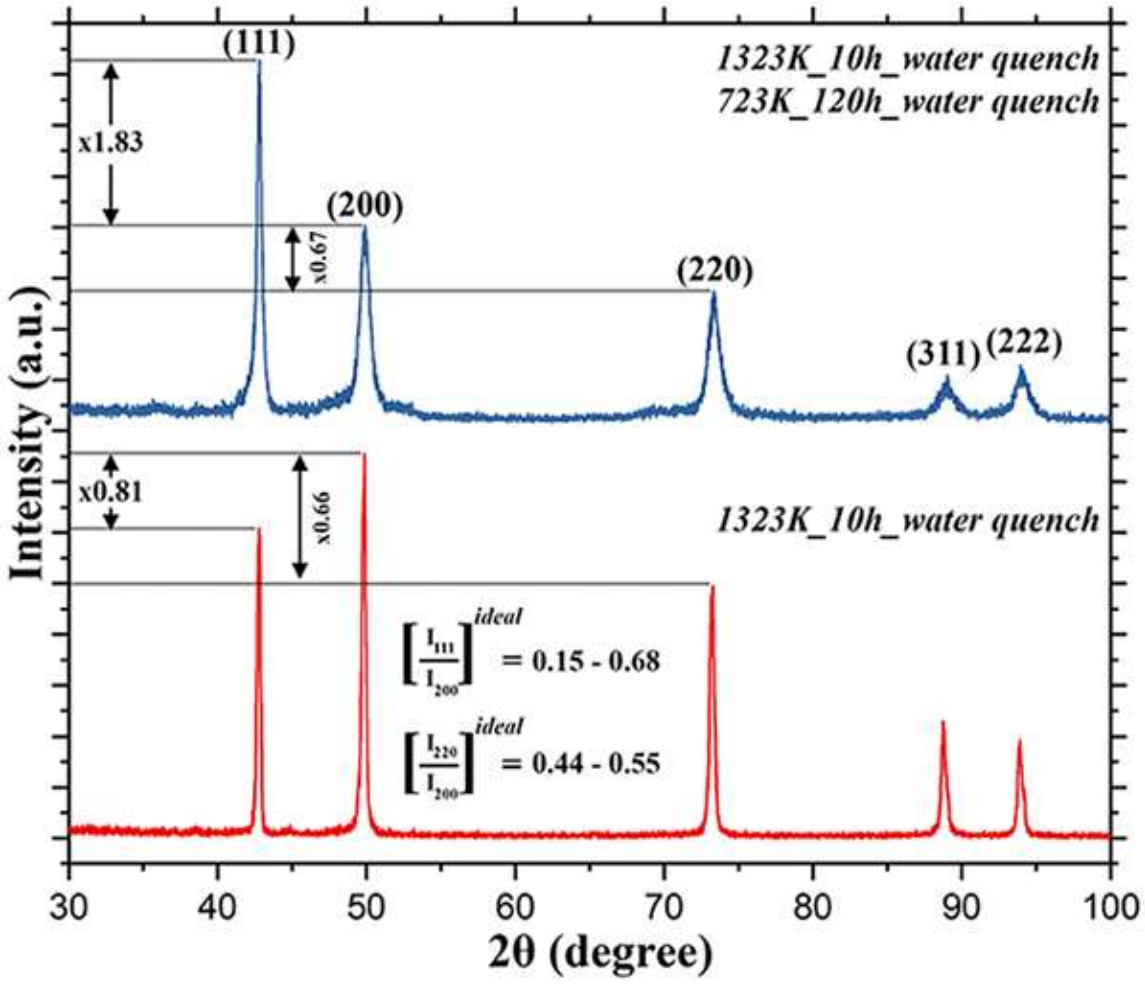

Figure 4.9: XRD patterns of (CoCuMgNiZn) ESO after sintering at 1323 K for 10 h followed by water quenching (in red) and after sintering at 1323 K for 10 h followed by ageing at 723 K for 120 h followed by water quenching (in blue). Anomalous intensity distribution and broadening of diffraction peaks after ageing is evident in the ESO.

The domain boundaries are thick and appearance of δ-fringes at the boundaries indicates that the domain walls are tilted with respect to the electron beam. The domains are formed after ageing and they grow to a size of ~15-25 nm after 120 h of holding, which clearly indicates that the growth kinetics of such domains is quite sluggish. In the dark field image (Figure 4.10d) with 020 spot lights up some of the boundaries. The domain wall boundaries are likely to be a variant of 020 type of planes. The growth of such domain walls, its implication on the stability of the single cubic rocksalt phase of this ESO will be discussed in the discussion section.

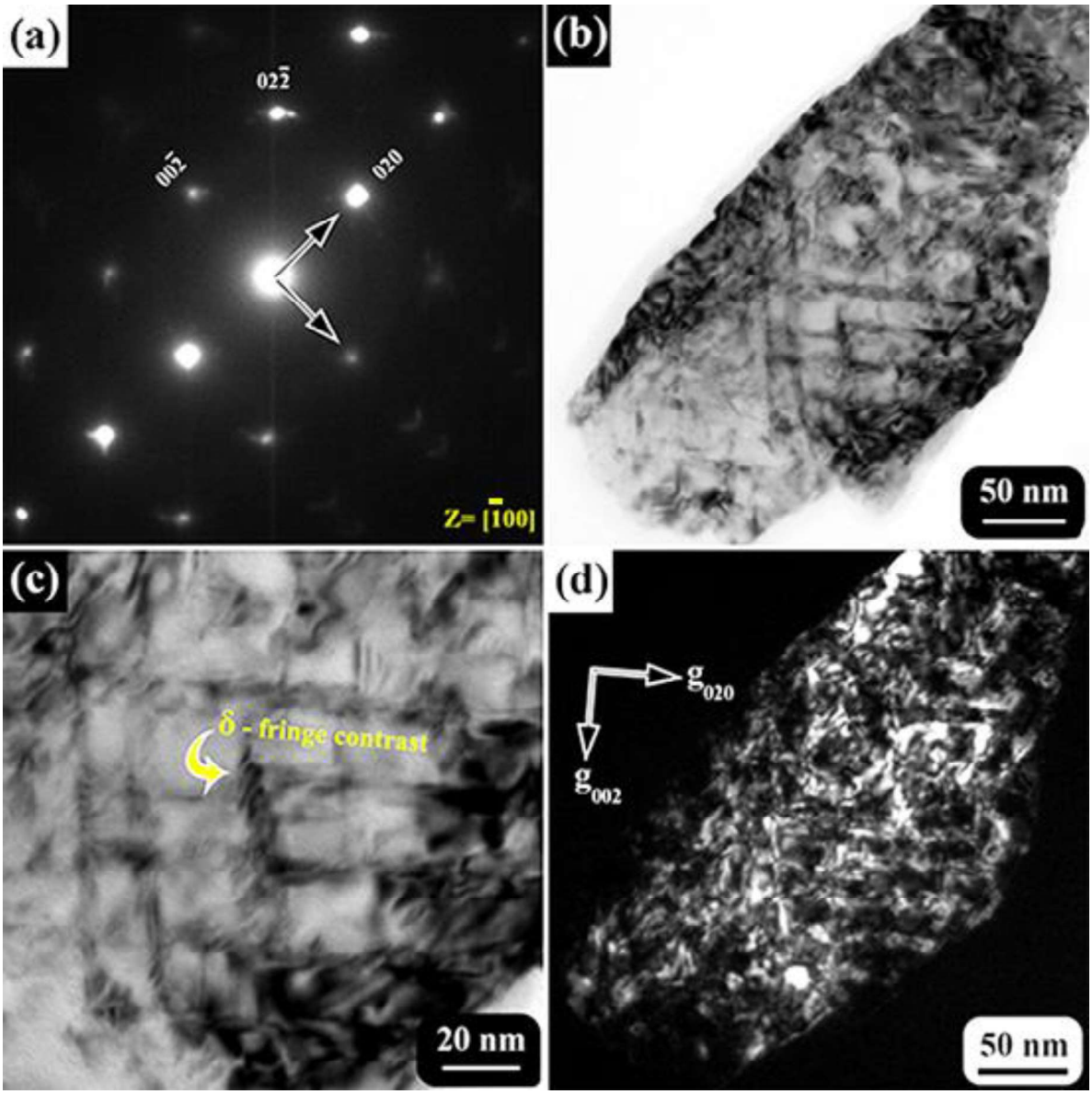

Figure 4.10: (a) z=[1̄00] electron diffraction pattern, TEM (b-c) bright field images and (d) dark field image of (CoCuMgNiZn) ESO after sintering at 1323 K for 10 h, subsequent ageing at 723 K for 120 h followed by water quenching. In the diffraction pattern in (a), asymmetrical diffused streaking of spots, splitting of spots is observed. In the bright field images (b-c) domain like structure with domain wall boundaries are observed. The domain wall boundaries are lightened up in the dark field image in (d) with g=020 diffraction spot.

Selected area electron diffraction pattern from a different region of the (CoCuMgNiZn) ESO after sintering at 1323 K for 10 h followed by ageing at 723 K for 120 h and water quenching is given in Figure 4.11(a-b). Both the diffraction patterns in Figure 4.11 are one and the same, however, one is inverted with respect to the other. In the diffraction pattern, modulation of intensity of the spots with occasional diffuseness is observed. All the principal reflections, their corresponding d-spacings, angular relations and the ratio of the principal vectors are given in Figure 4.11a. The diffraction pattern cannot be indexed consistently only with a cubic rocksalt phase with disordered cation distribution. The reflections connected with green dotted lines in the shape of a distorted hexagon corresponds to the [011] zone axis pattern of a cubic rocksalt phase with *a~4.22 Å* lattice parameter. In that case, the rocksalt phase is ordered along [200] and [022] type of directions. However, extra diffused intensity of 200 and 022 type of spots indicates that there is a likelihood of another correlated phase being present. The reflections connected with dotted yellow line in the form of a rectangle may be indexed to $[\bar{1}12]$ zone axis pattern of a cubic spinel phase with *a~8.15 Å* lattice parameter. In that situation, there is a specific orientation relationship between the cubic rocksalt phase and the cubic spinel phase with random cation distribution. The orientation relationships are $[\bar{1}12]_{Spinel} \parallel [011]_{Rocksalt}$ and $[220]_{Spinel} \parallel [0\bar{2}2]_{Rocksalt}$. There is a possibility that the cubic rocksalt phase is ordered and/or cubic spinel phase has grown locally with a specific orientation relationship with the rocksalt phase. The structural and thermodynamic implication of such observation will be discussed in the discussion section.

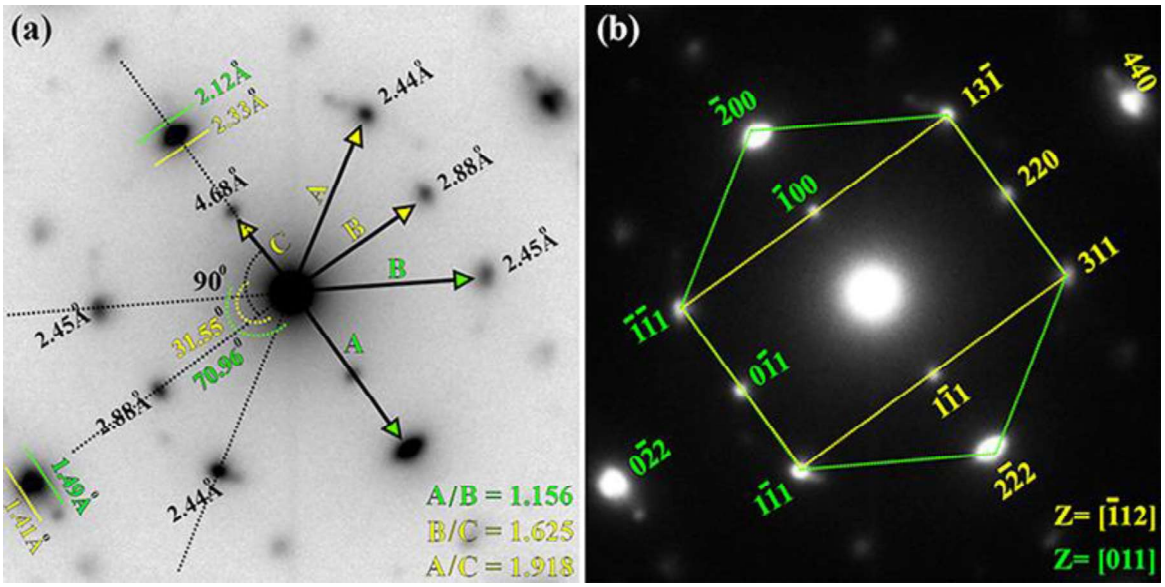

Figure 4.11: (a-b) Electron diffraction patterns from a different region of (CoCuMgNiZn) ESO after sintering at 1323 K for 10 h, subsequent ageing at 723 K for 120 h followed by water quenching. The diffraction pattern in (a) is inverted with respect to the diffraction pattern in (b). The patterns may be indexed with co-existent rocksalt phase and a spinel phase with a definite orientation relationship. The d-spacings, angular relationships and ratio of principal vectors are marked in (a). In (b) the diffraction spots corresponding to a rocksalt phase and a spinel phase are marked with different colours. The diffraction spots are connected with differently coloured dotted lines to bring out the zone axes symmetry shapes.

4.4. Discussion

Equimolar (CoCuMgNiZn) ESO is the first ever reported high entropy oxide in this class of new engineering materials, which is known to be stable in single phase rocksalt structure with random cation distribution and uniform chemistry [12]. The novel properties of this class of materials are sensitive to the structure and chemistry at the atomic scale [17, 25]. The properties have been explored with a general assumption that the structure and chemistry is uniform with absolutely random cation distribution. In the present study, the ESO has been systematically explored by XRD and electron microscopy in order to revisit its stability in the temperature-composition space. The evidences, when jotted down together, brings out a unified picture that clearly indicates the presence of very small structural domains with subtle variation of chemistry and oriented intergrowth of phases. It

may be directly related to the thermodynamic stability, kinetics of evolution of the microstructure, which will be discussed in the following sections.

4.4.1. Single phase and uniform chemistry of (CoCuMgNiZn) ESO

Over the last decade several high entropy oxides with multiple cation or anion disordering in their respective sublattices have been reported in literature [1-2, 26]. Single phase cubic rocksalt structure with uniform chemistry in (CoCuMgNiZn) ESO was the first ever high entropy oxide synthesized and characterized that initiated the excitement in this field [12]. Through XRD studies, the cubic rocksalt phase in this ESO has been reported. The shouldering or splitting that is observed in the XRD pattern has been attributed to the diffraction of Cu-$K_{\alpha I}$ and Cu-$K_{\alpha II}$ radiation [17]. In the present study, (CoCuMgNiZn) ESO after sintering at 1323 K for 10 h in pellet and powder form has been characterized by XRD with Co-K_{α} radiation. The diffraction pattern (Figure 4.1a) may be indexed to a cubic rocksalt structure with $a \sim 4.24$ Å lattice parameter. The shouldering may be attributed to the diffraction by Co-$K_{\alpha I}$ and Co-$K_{\alpha II}$ radiations. However, similar shouldering or splitting may also arise due to polymorphic transformation or local variation of chemistry. In order to explore the possibility of diffraction by Co-$K_{\alpha I}$ and Co-$K_{\alpha II}$ radiations, experimentally observed split between the peaks has been compared with the theoretically expected split between the peaks, which is given in Table 4.1. It is consistently observed for all allowable reflections that the experimentally observed split between the peaks is ~1.5-2.0 times higher than the theoretically expected separation between the peaks. Similar experiments have been done for the same ESO after sintering at 1323 K for 10 h, 100 h followed by water quenching and sintering at the same temperature followed by furnace cooling. However, for these samples, XRD experiments have been done with Cu-K_{α} radiation. In conformity with the earlier publications [17], shouldering and peak splitting is observed in these experiments also (Figure 4.2). However, the experimentally observed split between

the peaks is consistently ~1.5-2.5 times higher than the theoretically expected split due to the diffraction by Cu-$K_{\alpha I}$ and Cu-$K_{\alpha II}$ radiations (Table 4.1). It may be concluded from this experimental observation and theoretical calculation that the shouldering and splitting in the XRD pattern is not likely due to the diffraction either by Co-K_α or Cu-K_α doublets. The possibility of local polymorphic transformation with or without associated local modulation of chemistry should be explored.

Table 4.1: Theoretically calculated peak positions, the expected separation between $K_{\alpha I}$ and $K_{\alpha II}$ peaks and their relative comparison with the experimentally observed split between the peaks in (CoCuMgNiZn) ESO. The values are truncated after 3rd place of decimal without approximation.

$\lambda_{Co\ K\alpha I}$ = 1.789 Å, $\lambda_{Co\ K\alpha II}$ = 1.792 Å; $\lambda_{Cu\ K\alpha I}$ = 1.541 Å, $\lambda_{Cu\ K\alpha II}$ = 1.544 Å

Plane	d-spacing (Å)		$2\theta_B$ (°)		$2\theta_B$ (°)		$2\Delta\theta_B$ (°)			
	Co K_α	Cu K_α	Co $K_{\alpha I}$	Cu $K_{\alpha I}$	Co $K_{\alpha II}$	Cu $K_{\alpha II}$	Experimental		Theoretical	
(111)	2.445	2.447	42.919	36.623	42.995	36.745	0.107	0.122	0.076	0.074
(200)	2.117	2.12	49.988	42.551	50.078	42.761	0.129	0.21	0.090	0.086
(220)	1.497	1.497	73.386	61.825	73.530	62.065	0.202	0.24	0.144	0.134
(311)	1.277	1.276	88.930	74.082	89.118	74.365	0.261	0.283	0.188	0.168
(222)	1.223	1.222	94.008	77.966	94.213	78.291	0.284	0.325	0.205	0.182

There are several indirect evidences in the XRD patterns of the ESO after different types of thermal treatments that polymorphic transformation associated with local compositional modulations leads to the broadening, shouldering and splitting of peaks with non-ideal intensity ratio. In the XRD pattern with Co-K_α radiation of the pellet and the powder of (CoCuMgNiZn) ESO after sintering at 1323 K for 10 h followed by water quenching, non-

ideal intensity ratio has been observed (Figure 4.1a). Similar non-ideal intensity ratio with Cu-K_α radiation has been observed in the same ESO after different thermal treatments (Figure 4.2 and Figure 4.9). In earlier literature departure from ideal intensity ratio of the diffraction peaks has been attributed to the thermal history of the ESO along with Jahn-Teller distortion induced changes in the structure [23-24].

In the present study, in the SEM-XEDS maps (Figure 4.3) local variation of chemistry associated with the enriched and depleted regions of Mg and Cu has been observed. This further reinforces the idea of local polymorphic transformations with associated chemical modulation in this ESO. The XRD peaks of ESO after sintering at 1323 K for 10 h followed by water quenching (Figure 4.1(b-c)) may be deconvoluted to a number of peaks, which resemble after the d-spacings of the precursor oxides. Similar observation holds good for all other XRD patterns of the ESO with different thermal history. Moreover, longer h of exposure at high temperature (Figure 4.2 and Figure 4.9) leads to the reduction in total integrated intensity of the XRD peaks along with broadening. This observation is counter intuitive so far grain growth and stress relaxation in the grains is concerned. However, it definitely points to the formation of local structural domains with or without variation in chemistry. This statement may further be supported by the observation of tweeds within the grain body of the ESO along with shape evolution and diffused streaking of the diffraction spots (Figure 4.5 and Figure 4.6).

4.4.2. Structural modulation induced tweed formation and strain minimization

In the bright field images of the ESO, after sintering at 1323 K for 10 h, tweed formation within the grain body is observed. The tweeds are discontinuous that form ~5-15 nm domains (Figure 4.5). The corresponding electron diffraction patterns conform to a cubic

rocksalt structure with *a~4.23 Å* lattice parameter. However, diffused intensity around the spots with diffused streaking, spot splitting and evolution of shapes with modulation of intensity may be observed (Figure 4.6). When the extreme ends of the intensity modulated diffraction spots are connected with dotted lines, approximately [100] zone axis symmetry shapes of a cubic rocksalt structure are observed (Figure 4.6a). It may further be deduced that the symmetry shapes belong to two groups with different *c/a* ratios, which are rotated with respect to one another (Figure 4.7a). Experimentally observed diffraction pattern in Figure 4.6a may be generated schematically by superimposing the symmetry shapes in Figure 4.7a. Combined observation of this diffraction pattern along with tweed formation within the grain body clearly indicates the formation of local structural domains within the ESO. Structural domains may be associated with local variation of chemistry. However, it cannot be confirmed as the chemical variation may be random and finite thickness of the sample renders it impossible to associate one domain with a particular chemistry even by a fine probe technique as domains with different chemistry are stacked together along the thickness of the sample.

In a different region of the ESO, after sintering at 1323 K for 10 h, arcing of spots with finite intensity modulation is observed (Figure 4.8). It may further be deduced from the diffraction patterns that structural domains are formed with mutual in-plane and out-of-plane rotation that leads to the arcing of the diffraction spots. In the corresponding bright field images linear fringe contrast is observed (Figure 4.8). After ageing the ESO for long h, growth of such domains with clear domain walls is observed (Figure 4.10). Similar domain formation with in-plane and out-of-plane rotation leading to a helical structure of domains has been observed in (CaCoFeMgNi) multicomponent oxide [27].

Mutually rotated domain formation that appears as tweed or two-dimensional fringes is schematically presented in Figure 4.12a. In this figure, local composition modulation has

been assumed to be the driving mechanism that leads to local structural variation. Local structural variation helps in relaxing the lattice strain that is manifested due to the presence of multiple cations in the same lattice. However, in order to minimize the interfacial strain, the local structurally modulated domains rotate with respect to one another.

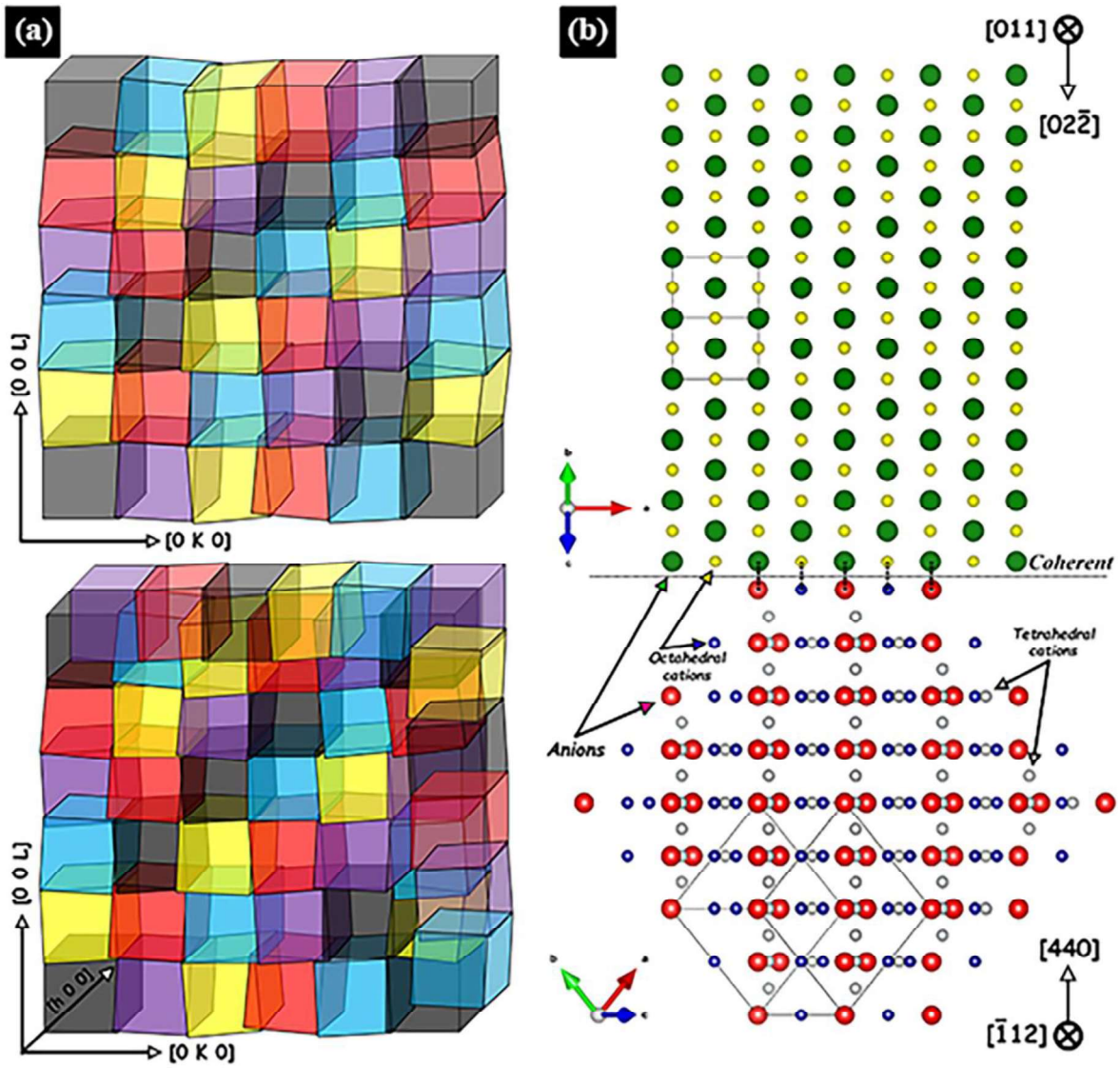

Figure 4.12: (a) Schematic representation of structurally modulated domains in 2D and in 3D in the (CoCuMgNiZn) ESO. Structural modulation may be initiated with the chemical modulation in individual domains, which are represented with different colours. Structural modulation in 3D makes the ESO appear as uniform in chemistry due to the overlap of domains with different chemistry. (b) Schematic representation of oriented growth of rocksalt phase and a spinel phase. The interface is coherent.

The assumed local chemical variation leading to local structural modulation is presented with different colours of the domains in the schematic in Figure 4.12a. Such domains grow further with ageing. However, the growth kinetics is sluggish. Chemical modulation of such domains is quite difficult, if not impossible, to capture through fine probe imaging and spectroscopy techniques as the domains are randomly distributed and due to the finite thickness of the sample, domains with different chemistry may stack up one on the top of other. As the interaction volume of the probe is not restricted within one domain, the domains will always reveal uniform average chemistry of the ESO.

The (CoCuMgNiZn) ESO after sintering at 1323 K for 10 h followed by ageing at 723 K for 120 h and quenching shows oriented growth of spinel domains in the rocksalt structure (Figure 4.11). There is a possibility of cation ordering in the rocksalt structure along <200> and <022> type directions. There is a specific orientation relationship between the rocksalt phase and the spinel phase. Rocksalt and spinel phase are structurally quite correlated as in the rocksalt phase all the octahedral voids are filled out and in the spinel phase only alternate octahedral voids are filled out. There is a good possibility that spinel phase grows within the rocksalt phase locally in an oriented manner. The interface structure of the rocksalt phase with the spinel phase with the observed orientation relationship is schematically presented in Figure 4.12b. It is observed from the crystal structure diagram that the interface between the rocksalt phase and the spinel phase is coherent that assures minimal interface strain. Similar coherent and semi coherent interface formation through oriented growth of phases has been observed in (CaCoFeMgNi) multicomponent oxide after different heat treatments [27].

It is worth pointing out that the (CoCuMgNiZn) ESO after sintering at 1323 K for 10 h, 100 h followed by water quenching and furnace cooling shows definite changes in the XRD patterns (Figure 4.2). There is a reduction in the total integrated intensity of the peaks with

finite broadening after longer h of heat treatment, which might be associated with the local chemical variation leading to a modulation in d-spacings. A finite leftward shift of the peaks is also observed after longer h of heat treatment. Left shift of the peaks indicates increase in the d-spacings and increase in the lattice parameter and volume of the crystal. This may be associated with the volumetric stress relaxation of the crystal with longer h of exposure at high temperature. The structure of the ESO is cubic rocksalt with *a~4.22 Å* lattice parameter. In the rocksalt structure, oxygen ions form the FCC lattice and the cations are octahedrally located. Assuming [110] direction to be the closest packed direction, the relationship between the lattice parameter *'a'* and the radius of the oxygen ion *'r'* is $4r=\sqrt{2}a$ and the size of the octahedral void V_r may be written as $V_r= (\sqrt{2}-1)r$. Based on this calculation, the maximum size of cation that may be accommodate in the octahedral void is ~62 pm. However, the size of Co^{2+}, Cu^{2+}, Mg^{2+}, Ni^{2+}, Zn^{2+} at octahedral coordination are ~75 pm, ~73 pm, ~72 pm, ~69 pm and ~74 pm respectively. Size of the octahedral cations being larger than the octahedral size, accommodation of the cations in the octahedral voids leads to the generation of volumetric stress. High temperature exposure for longer time provides the required stimuli to release the volumetric stress by increasing the average lattice parameter of the crystal and the volume. Further, local modulation helps in reducing the lattice strain.

It may be summed up from the above discussion that the ESO with random distribution of cations always attempts to reduce its strain field provided an external energy stimulus is obtained. Local chemical modulation, variation in d-spacings and increase in lattice parameter helps in reducing the volumetric stress and lattice strain, which is manifested in broadening of x-ray diffraction peaks, diffused intensity around the electron diffraction spots and its shape evolution, arcing of the diffracted spots and tweed/domain formation in the grain body. Local structural variation induced by local chemical modulation leads to

the formation of interfacial strain between the tweeds and the domains. Mutual rotation, interpenetration of domains/tweeds and oriented growth of correlated phases with coherent/semi-coherent boundaries helps in accommodating the interfacial strain. Very similar observation in case of (CaCoFeMgNi) multicomponent oxide [27] further reinforces the mechanism of strain minimization in multicomponent ESOs.

4.4.3. Thermodynamic implications of strain minimization and stability of ESO

High entropy oxide (HEO), an important member in the family of high entropy materials (HEMs), is said to be entropy stabilized by random distribution of cations in the cation sublattice [2, 15, 22]. It is believed that random distribution of five or more cations increases the configurational entropy so much that free energy of the system is always dominated by the entropic contribution irrespective of enthalpy of formation of such oxides [28]. This has led to the new name of this class of materials as entropy stabilized oxide (ESO) [12]. Equimolar (CoCuMgNiZn) oxide is the first ever reported high entropy oxide that is believed to be stabilized in a cubic rocksalt structure in the time-temperature space. It is also widely reported that the presence of five cations makes the lattice quite strained [15].

In the present study, fine scale composition segregation between Cu and Mg ions has been observed in a subtle way. Additionally, the tendency of the system to reduce its volumetric strain, lattice strain and interfacial strain has been observed through the formation of tweeds, inter-grown domains and oriented growth of structurally correlated phases with or without compositional modulation. Though entropy remains to be the single most dominating factor in deciding the stability of the phase in time-temperature space, other

factors should also be taken into account in order to understand the thermodynamic stability issue of the material.

Change in Gibbs free energy is given by $\Delta G = \Delta H - T\Delta S$, where the symbols have their usual meaning. Further, $\Delta H = \Delta U + P\Delta V$ for a constant pressure process. The term $P\Delta V$ may be considered to be the change in the mechanical energy in the process. A qualitative look in the above equations indicates that the presence of five or more cations in the same sublattice will make the configurational entropy very high. However, it will definitely increase the strain energy in the crystal. $-T\Delta S$ term will always have a negative contribution and the strain energy term ($P\Delta V$) will always have a positive contribution to the Gibbs free energy change. Formation of local compositionally modulated domains will reduce the negative contribution of $-T\Delta S$ term, however, the reduction of volumetric strain, lattice strain and interfacial strain through the formation of tweeds, inter-grown domains and oriented growth of structurally correlated phases will reduce the positive contribution of the $P\Delta V$ term. Combined interplay of these two terms should negatively maximize the change in Gibbs free energy. It is understood that the stability of such multicomponent oxides is not solely determined by the entropy. However, it is a combined interplay of entropy and strain energy. Similar behaviour has been observed in case of (CaCoFeMgNi) multicomponent oxide [27].

4.5. Conclusions

It may be concluded from the present study that first ever reported (CoCuMgNiZn) ESO forms a cubic rocksalt structure with $a \sim 4.22$ Å lattice parameter. However, the shouldering or splitting of peaks in XRD, hitherto which has been understood as the diffraction from Cu-K_α or Co-K_α doublets, may not be correct. The shouldering, splitting and non-ideal intensity distribution should be attributed to local structural modulation in the ESO, accompanied with local compositional variation. The rocksalt phase in the ESO reduces its

volumetric strain, lattice strain and interfacial strain by tweed formation and sluggish growth of the tweeds in the form of domains that separates several structurally modulated domains within the rocksalt phase. Oriented growth of structurally correlated phases with coherent/semi-coherent interfaces further reduces the strain in the ESO. The stability of the ESO is not solely determined by the maximization of configurational entropy. However, it is the trade-off between the configuration entropy and different types of strain energy that determines the stability of the phase in time-temperature space.

4.6. Reference

1. C. Oses, C. Toher, S. Curtarolo, High-entropy ceramics, Nat. Rev. Mater., 2020, 5, 295-309.
2. M. Brahlek, M. Gazda, V. Keppens, A. R. Mazza, S. J. McCormack, A. Mielewczyk-Gryn, B. Musico, K. Page, C. M. Rost, S. B. Sinnott, C. Toher, T. Z. Ward, A. Yamamoto, What is in a name: Defining “high entropy” oxides, APL Mater., 2022, 10, 110902-11.
3. Z. Lun, B. Ouyang, D. H. Kwon, Y. Ha, E. E. Foley, T. Y. Huang, Z. Cai, H. Kim, M. Balasubramanian, Y. Sun, J. Huang, Y. Tian, H. Kim, B. D. McCloskey, W. Yang, R. J. Clement, H. Ji, G. Ceder, Cation-disordered rocksalt-type high-entropy cathodes for Li-ion batteries, Nat. Mater., 2021, 20, 214-221.
4. Q. Wang, A. Sarkar, Z. Li, Y. Lu, L. Velasco, S. S. Bhattacharya, T. Brezesinski, H. Hahn, B. Breitung, High entropy oxides as anode material for Li-ion battery applications: A practical approach, Electrochemistry Communications, 2019, 100, 121-125.
5. D. Berardan, S. Franger, A. K. Meena, N. Dragoe, Room temperature lithium superionic conductivity in high entropy oxides, J. Mater. Chem. A, 2016, 4, 9536-9541.
6. A. Sarkar, L. Velasco, D. Wang, Q. Wang, G. Talasila, L. de Biasi, C. Kubel, T. Brezesinski, S. S. Bhattacharya, H. Hahn, B. Breitung, High entropy oxides for reversible energy storage, Nature Communications, 2018, 9, 3400 (9 pages).
7. M. V. Kante, M. L. Weber, S. Ni, I. C. G. van den Bosch, E. van der Minne, L. Heymann, L. J. Falling, N. Gauquelin, M. Tsvetanova, D. M. Cunha, G. Koster, F.

Gunkel, S. Nemsak, H. Hahn, L. V. Estrada, C. Baeumer, A high-entropy oxide as high activity electrocatalyst for water oxidation, ACS Nano, 2023, 17, 5329-5339.

8. A. Sarkar, Q. Wang, A. Schiele, M. R. Chellali, S. S. Bhattacharya, D. Wang, T. Brezesinski, H. Hahn, L. Velasco, B. Breitung, High-entropy oxides: Fundamental aspects and electrochemical properties, Adv. Mater., 2019, 31, 1806236 (9 pages).
9. S. H. Albedwawi, A. Aljaberi, G. N. Haidemenopoulos, K. Polychronopoulou, High entropy oxides-exploring a paradigm of promising catalysts: A review, Materials and Design, 2021, 202, 109534 (27 pages).
10. S. Maiti, W. Steurer, Structural-disorder and its effect on mechanical properties in single-phase TaNbHfZr high-entropy alloy, Acta Mater., 2016, 106, 87-97.
11. Y. Zhang, T. T. Zuo, Z. Tang, M. C. Gao, K. A. Dahmen, P. K. Liaw, Z. P. Lu, Microstructures and properties of high-entropy alloys, Prog. Mater. Sci., 2014, 61, 1-93.
12. C. M. Rost, E. Sachet, T. Borman, A. Moballegh, E. C. Dickey, D. Hou, J. L. Jones, S. Curtarolo, J. P. Maria, Entropy-stabilized oxides, Nature Communications, 2015, 6, 8485 (8 pages).
13. G. Anand, A. P. Wynn, C. M. Handley, C. L. Freeman, Phase stability and distortion in high-entropy oxides, Acta Mater., 2018, 146, 119-125.
14. K. C. Pitike, K. C. Santosh, M. Eisenbach, C. A. Bridges, V. R. Cooper, Predicting the phase stability of multicomponent high-entropy compounds, Chem. Mater., 2020, 32, 7507-7515.
15. S. J. McCormack, A. Navrotsky, Thermodynamics of high entropy oxides, Acta Mater., 2021, 202, 1-21.
16. A. Sarkar, R. Djenadic, N. J. Usharani, K. P. Sanghvi, V. S. K. Chakravadhanula, A. S. Gandhi, H. Hahn, S. S. Bhattacharya, Nanocrystalline multicomponent entropy stabilized transition metal oxides, J. Eu. Ceram. Soc., 2017, 37, 747-754.
17. C. M. Rost, Z. Rak, D. W. Brenner, J. P. Maria, Local structure of the $Mg_xNi_xCo_xCu_xZn_xO$ (x=0.2) entropy-stabilized oxide: An EXAFS study, J. Am. Ceram. Soc., 2017, 100, 2732-2738.
18. Y. Gu, A. Bao, X. Wang, Y. Chen, L. Dong, X. Liu, H. Pan, Y. Li, X. Qi, Engineering the oxygen vacancies of rocksalt-type high-entropy oxides for enhanced electrocatalysis, Nanoscale, 2022, 14, 515-524.

19. Z. Grzesik, G. Smola, M. Stygar, J. Dabrowa, M. Zajusz, K. Mroczka, M. Danielewski, Defect structures and transport properties in (Co, Cu, Mg, Ni, Zn)O high entropy oxide, J. Eu. Ceram. Soc., 2019, 39, 4292-4298.
20. W. Hong, F. Chen, Q. Shen, Y. H. Han, W. G. Fahrenholtz, L. Zhang, Microstructural evolution and mechanical properties of (Mg, Co, Ni, Cu, Zn)O high-entropy ceramics, J. Am. Ceram. Soc., 2019, 102, 2228-2237.
21. A. D. Dupuy, M. R. Chellali, H. Hahn, J. M. Schoenung, Nucleation and growth behavior of multicomponent secondary phases in entropy-stabilized oxides, J. Mater. Res., 2023, 38, 198-214.
22. M. Fracchia, M. Coduri, M. Manzoli, P. Ghigna, U. A. Tamburini, Is configurational entropy the main stabilizing term in rock-salt $Mg_{0.2}Co_{0.2}Ni_{0.2}Cu_{0.2}Zn_{0.2}O$ high entropy oxide, Nature Communications, 2022, 13, 2977 (4 pages).
23. D. Berardan, A. K. Meena, S. Franger, C. Herrero, N. Dragoe, Controlled Jahn-Teller distortion in (MgCoNiCuZn)O-based high entropy oxide, J. Alloys Comp., 2017, 704, 693-700.
24. Z. Rak, J. P. Maria, D. W. Brenner, Evidence for Jahn-Teller compression in the (Mg, Co, Ni, Cu, Zn)O entropy-stabilized oxide: A DFT study, Mater. Lett., 2018, 217, 300-303.
25. C. M. Rost, D. L. Schmuckler, C. Bumgardner, M. S. B. Haque, D. R. Diercks, J. T. Gaskins, J. P. Maria, G. L. Brennecka, X. Li, P. E. Hopkins, On the thermal and mechanical properties of $Mg_{0.2}Co_{0.2}Ni_{0.2}Cu_{0.2}Zn_{0.2}O$ across the high entropy to entropy-stabilized transition, APL Mater., 2022, 10, 121108 (6 pages).
26. B. L. Musico, D. Gilbert, T. Z. Ward, K. Page, E. George, J. Yan, D. Mandrus, V. Keppens, The emergent field of high entropy oxides: Design, prospects, challenges and opportunities for tailoring material properties, APL Mater., 2020, 8, 040912 (16 pages).
27. S. Mukherjee, N. K. Mukhopadhyay, J. Basu, Composition modulation, strain minimization and oriented growth of phases in equimolar (CaCoFeMgNi) multicomponent oxide, Acta Mater., 2025, 285, 120621 (12 pages).
28. M. Fracchia, M. Coduri, P. Ghigna, U. A. Tamburini, Phase stability of high entropy oxides: A critical review, J. Eu. Ceram. Soc., 2024, 44, 585-594.